Research Article

Lian Wu, Yongqiang Dai, Wei Zeng, Jintao Huang, Bing Liao, and Hao Pang*

Effective ion pathways and 3D conductive carbon networks in bentonite host enable stable and high-rate lithium–sulfur batteries

https://doi.org/10.1515/ntrev-2021-0005
received January 26, 2021; accepted February 5, 2021

Abstract: Fast charge transfer and lithium-ion transport in the electrodes are necessary for high performance Li–S batteries. Herein, a N-doped carbon-coated intercalated-bentonite (Bent@C) with interlamellar ion path and 3D conductive network architecture is designed to improve the performance of Li–S batteries by expediting ion/electron transport in the cathode. The interlamellar ion pathways are constructed through inorganic/organic intercalation of bentonite. The 3D conductive networks consist of N-doped carbon, both in the interlayer and on the surface of the modified bentonite. Benefiting from the unique structure of the Bent@C, the S/Bent@C cathode exhibits a high initial capacity of 1,361 mA h g^{-1} at 0.2C and achieves a high reversible capacity of 618.1 m Ah g^{-1} at 2C after 500 cycles with a sulfur loading of 2 mg cm^{-2}. Moreover, with a higher sulfur loading of 3.0 mg cm^{-2}, the cathode still delivers a reversible capacity of 560.2 mA h g^{-1} at 0.1C after 100 cycles.

Keywords: Ion transport pathways, conductive carbon networks, bentonite, cathode materials, lithium–sulfur batteries

* **Corresponding author: Hao Pang,** Guangdong Provincial Key Laboratory of Industrial Surfactant, Institute of Chemical Engineering, Guangdong Academy of Sciences, Guangzhou 510665, China, e-mail: panghao@gic.ac.cn, tel: +86-20-3237-6449, fax: +86-20-3237-3106
Lian Wu, Yongqiang Dai, Wei Zeng: Guangdong Provincial Key Laboratory of Industrial Surfactant, Institute of Chemical Engineering, Guangdong Academy of Sciences, Guangzhou 510665, China
Jintao Huang: Department of Polymeric Materials and Engineering, School of Materials and Energy, Guangdong University of Technology, Guangzhou 510006, China
Bing Liao: Guangdong Academy of Sciences, Guangzhou 510070, China

1 Introduction

With the increasing energy demands of portable electronic devices, electric vehicles, and grid storage, the development of novel reliable battery systems with high energy density is of great significance. Among the existing chemical battery systems, lithium-ion batteries have attracted worldwide attention due to the advantages of high voltage, high energy density, good safety performance, and long cycle life [1]. However, a key shortcoming of the existing lithium-ion batteries is their limited energy density (~400 W h kg^{-1}). In contrast, lithium–sulfur (Li–S) batteries offer high theoretical specific capacity (1,675 mA h g^{-1}) and high energy density (2,600 W h kg^{-1}) [2], and thus have attracted more interest in recent years. However, the commercialization of Li–S batteries has been hindered by several technical challenges, especially the following two critical issues [3]: (i) the insulating nature of sulfur and its discharging products (Li_2S/Li_2S_2) limits charge transfer in the cathode and leads to low utilization efficiency of the active material; and (ii) the dissolution and shuttling of the soluble polysulfides (LiPSs:Li_2S_x, $4 \le x \le 8$) formed during the cycling process, known as the "shuttle effect," result in a low coulombic efficiency and severe capacity fading. Therefore, the poor electronic conductivity of sulfur cathodes and the "shuttle effect" are crucial issues that urgently need to be settled for the development of Li–S batteries. Moreover, high sulfur loading cathodes are essential for realizing high energy density Li–S batteries, and fast charge transfer and lithium-ion transport are indispensable to enable the practical application of high sulfur loading cathodes in electric vehicles and stationary electric grids [4].

The design of porous or/and layered architectures with good conductivity and LiPSs adsorption capabilities is proposed as the main approach to tackle the aforementioned issues and facilitate lithium-ion transport [5]. Hence, porous carbon materials (e.g., carbon nanotubes [6], meso- and microporous carbons [7,8]), metal-organic frameworks

(MOFs) [9], layered metal oxides [10], MXenes [11], fluorinated carbon [12], and so forth have been widely studied as sulfur hosts for improving the capacity and cyclic/rate performance of Li–S batteries. Although many of these materials exhibit good performances as sulfur hosts, the lithium-ion diffusion rate and LiPSs conversion kinetics in high sulfur loading cathodes are still unsatisfactory. In addition, the high cost and complex preparation processes involved also limit their applications. Recently, researchers have been exploring natural clay minerals (e.g., bentonite [13], halloysite [14], and vermiculite [15]) as sulfur hosts, and impressive achievements were obtained. Especially, as a class of naturally existing two-dimensional (2D) materials, bentonite has numerous advantages, such as low cost, widespread abundance, and environmental friendliness. In addition, bentonite possesses a large interlayer space and a high adsorption capacity [16], which makes it a potential ideal sulfur host. As for its structure, bentonite consists of solid 2D layers, and each layer includes two silica tetrahedral sublayers sandwiching a central alumina octahedral sublayer; between these layers, van der Waals forces are formed with hydrated cations balancing the charge [17]. This unique structure can facilitate fast Li ion transport. Recent research reports from He's group have demonstrated that the orderly layered structure of lithium-bentonite provides an atomic interlamellar ion path which is highly desirable in electrodes and separators, resulting in rapid lithium-ion transport [18,19].

However, the poor conductivity of bentonite has limited its application in Li–S battery cathodes, which, to the best of our knowledge, is probably the main reason for the rarely successful attempts in improving the performance of Li–S batteries with bentonite as a sulfur host. Moreover, current research has only focused on lithium-bentonite which has a smaller interlayer space than raw bentonite [13], implying that the ion transport pathways are very narrow and the lithium-ion diffusion barrier still needs to be further reduced to obtain a faster lithium-ion transport.

Carbon materials have been widely explored for batteries due to their chemical inertness, high electron conductivity, facile control over transformation from amorphous to crystalline structure, and low synthesis cost [20].

Inspired by the above consideration, herein, the interlamellar pore structure of bentonite is regulated through traditional inorganic/organic intercalation modification methods, and polydopamine (PDA) is coated onto the modified bentonite. Subsequently, the organic intercalation agent and PDA are simultaneously carbonized for *in situ* synthesis of nano conductive carbon materials not only on the surface, but also in the interlayers of bentonite. Through this approach, a N-doped carbon-coated intercalated-bentonite composite sulfur host (denoted as Bent@C) with efficient ion transport pathways and interconnected three-dimensional (3D) conductive networks can be controllably constructed. This strategy delivers the following advantages:

(i) Through regulating the interlayer distance of bentonite by simple inorganic/organic intercalation, a fast lithium-ion transport pathway can be constructed
(ii) The organic intercalation agent-derived carbon in the interlayer combines with PDA-derived carbon (PDA-C) on the surface, endowing Bent@C with an interconnected 3D conductive network which effectively improves the conductivity of this composite bentonite host
(iii) The alumina-silicate components of bentonite clay and abundant N-doping of the carbon conductive networks provide a strong chemical adsorption of LiPSs
(iv) This synthetic route is both facile and economical, and thus highly suitable for large-scale production. As a result, the obtained S/Bent@C cathode can exhibit significantly improved electrochemical performance. Furthermore, this work provides an economical and effective strategy for the construction of efficient ion transport pathways and conductive networks in high sulfur loading cathodes by using 2D layered clay materials.

2 Experimental

2.1 Synthesis of inorganic/organic intercalated-bentonite

In order to prepare inorganic/organic intercalated-bentonite, a pillaring solution of Al Keggion ions (hydroxy-aluminum oligomeric cations, $[Al_{13}O_4(OH)_{24}\cdot(H_2O)_{12}]^{7+}$, denoted as Al_{13}) was first prepared by slowly adding a 0.2 M NaOH solution to a 0.2 M $AlCl_3$ solution under constant stirring at 60°C until the OH^-/Al^{3+} ratio reached a value of 2.4 [21]. The resultant solution was subsequently stored at 60°C for two days. The organic intercalation solution of chitosan (CS) was prepared by dissolving chitosan (deacetylation degree of 95%, average molecular weight of 60,000 Da) in a 1% (v/v) aqueous acetic acid solution at a concentration of 1 wt% with stirring for 6 h [22]. Meanwhile, cation exchange was carried out for raw bentonite to prepare lithium-bentonite (Li-Bent).

Typically, the raw bentonite (with a cation exchange capacity (CEC) of 91 mmol (100 g^{-1})) was treated with 0.5 M H_2SO_4 solution at 60°C for 2 h for full protonation to obtain active bentonite. The active bentonite was then converted to Li-Bent via treatment with 1 M LiOH at 60°C for 1 h [13]. After each cation exchange process, the obtained material was washed with deionized water (DI water) for three times. Finally, the prepared Li-Bent was added to DI water, forming a 2 wt% clay suspension with stirring for 2 h at 60°C, then the pillaring solution of Al_{13} (with the ratio of 10 mmol Al^{3+} g^{-1} bentonite) and the organic intercalation solution of chitosan (with the ratio of glucosamine (MW = 161 g mol^{-1}) among chitosan to the CEC of Li-Bent was 1:1) were simultaneously added dropwise into 100 mL of the clay suspension with stirring for 6 h at 60°C. After one day of aging, the prepared product was washed several times with DI water and vacuum dried at 80°C for 12 h to obtain dry inorganic/organic intercalated-bentonite (denoted as Al/CS-Bent) powder.

2.2 Synthesis of the carbon-coated intercalated-bentonite composites

PDA-coated intercalated-bentonite (denoted as Bent@PDA) was prepared according to a procedure reported in literature [23]. Typically, 1 g of Al/CS-Bent was ultrasonically dispersed in 200 mL of Tris-HCl buffer solution for 5 min. Dopamine hydrochloride (1 g) was dissolved in 100 mL of Tris-HCl buffer solution and then added dropwise into the above suspension under constant stirring at room temperature for 24 h with a stirring rate of 300 rpm. The mixture was subjected to filtration and the filtered product was washed several times with DI water and vacuum dried overnight at 60°C to obtain the Bent@PDA precursor. Subsequently, the Bent@PDA precursor was heated at 700°C for 2 h under an argon atmosphere at a heating rate of 5°C min^{-1} to produce the carbon-coated intercalated-bentonite composites (denoted as Bent@C).

2.3 Synthesis of the sulfur/Bent@C composites

The sulfur/Bent@C (S/Bent@C) composites were synthesized by a commonly used melt-diffusion method. The as-prepared Bent@C and sublimed sulfur were mixed with a weight ratio of 2:8 and homogenously ground for ~10 min. The mixture was then transferred into a sealed Teflon container that was filled with argon, and then heated in an oven at 155°C for 12 h. After cooling down, the obtained S/Bent@C was taken and homogenously ground for 20 min to form a uniform powder. For comparison, S/Li-Bent composite was also prepared via the same method.

2.4 Polysulfide adsorption tests

Li_2S and sublimed sulfur, with a molar ratio of 1:5, were dissolved in a mixed solvent of 1,2-dimethoxyethane/1,3-dioxolane (DME/DOL, 1:1 v/v) under vigorous stirring at 50°C to obtain the 0.05 M Li_2S_6 solution. Adsorption tests were performed to compare the adsorption capacities of Bent@C, Li-Bent, and PDA-C. Typically, 20 mg of adsorbent was added into 10 mL of the obtained Li_2S_6 solution, followed by stirring for 1 min and standing for 12 h. The resultant solutions were compared with pure Li_2S_6 solution in the glass vial.

2.5 Materials characterization

The morphological characterization and elemental mapping were performed via Scanning Electron Microscopy (SEM) using a Zeiss Sigma 300 system coupled with a Bruker XFlash6 X-ray energy dispersive spectroscopy (EDS). Transmission Electron Microscopy (TEM, FEI Talos F200s) was used to observe the carbon layer and the layered structure. The X-ray diffraction (XRD) patterns were recorded employing a high-power X-ray diffraction (XRD, D8 Rigaku 9000) system with Cu Kα radiation. Nitrogen adsorption and desorption isotherms were detected with a Micromeritics ASAP 2460 system at 77 K. Thermogravimetric (TG) analysis was performed using a TGA Q5000 analyzer over a temperature range from 20 to 600°C with a heating rate of 10°C min^{-1} in an N_2 atmosphere to determine the sulfur content of the composite cathodes. The Raman experiments were performed using a RM 2000 Microscopic Confocal Raman Spectrometer with a 532 nm laser. The chemical states of C, N, and S in the samples were determined by X-ray photoelectron spectroscopy (XPS, 250XI, EscaLab).

2.6 Electrochemical characterization

The composite cathodes were prepared by a traditional slurry coating method. Electrode materials, carbon black

(Super P) and polyvinylidene fluoride (PVDF), were uniformly mixed at a weight ratio of 7:2:1 in *N*-methyl pyrrolidone (NMP). The resulting slurry was then coated onto an aluminum foil and dried overnight in a vacuum oven at 60°C. Finally, the coated aluminum foil was cut into discs with a diameter of 12 mm to obtain electrodes. The areal sulfur loading was controlled from 1.2 to 3.0 mg cm^{-2}. For electrochemical measurements, CR2025 coin cells were assembled in a glove box that was filled with argon. Lithium foils and Celgard 2400 membrane were used as the anode and separator, respectively. The electrolyte was 1.0 M lithium bis(trifluoromethanesulphonyl) imide (LiTFSI) in the binary solvent consisting of 1,3-dioxolaneand (DOL) and 1,2-dimethoxyethane (DME) (1:1 by volume) with 2.0 wt% $LiNO_3$ as an additive. The electrolyte was added at a quantity of 15 µL per mg of sulfur. A multi-channel battery test system (NEWARE BTS-4000) was employed for the galvanostatic charge/discharge tests at different current densities within a cutoff voltage window of 1.7–2.8 V. Employing a zennium pro-electrochemical workstation, cyclic voltammetry (CV) measurements were conducted between 1.5 and 3.0 V at different scan rates, and electrochemical impedance spectroscopy (EIS) was performed by applying an AC amplitude of 5 mV in the frequency range of 0.01–10^5 Hz.

3 Results and discussion

3.1 Design and synthesis of the S/Bent@C material

A schematic illustration of the synthesis procedure for Bent@C host is displayed in Figure 1. The aluminosilicate sheets in raw bentonite are disordered as the cations contained in the interlayer (i.e., Na^+, Mg^{2+}, Ca^{2+}) are highly variable in size and distribution. For the synthesis, the cations in the interlayer of raw bentonite are first converted to Li^+ through a general ion exchange approach. As a result, the aluminosilicate sheets are converted from a disordered to an ordered structure [13]. An inorganic-organic intercalation modification is subsequently performed, during which Al Keggion ions and CS molecules are intercalated into the interlayer spaces to enlarge the basal spacing of the bentonite. The intercalated-bentonite is then coated with PDA through the self-polymerization of dopamine, followed by heat treatment at 700°C for 2 h. During heat treatment, the PDA coating film and the interlamellar CS are carbonized, forming N-doped carbon on the surface and in the interlayer of bentonite simultaneously, and the generated N-doped carbon can achieve a high electronic conductivity of 0.203 S cm^{-1} [24]. Therefore, an interconnected 3D carbon conductive network and an efficient ion transport pathway are controllably constructed. It is worth noting that the thermal stability of bentonite is greatly improved due to the aluminum pillared effect, so that it can bear high temperature treatment even above 700°C without any collapse of the aluminosilicate layered structure [21]. Hence, following the procedure demonstrated above, the Bent@C host material with a high electrical conductivity and fast lithium-ion transport pathways can be prepared. During the charge/discharge cycling processes, the carbon conductive network can facilitate electron transport, permitting the electrons to fully contact with the sulfur atoms, thus enhancing the specific capacity of the Li–S batteries. Meanwhile, the combination of the large basal spacing and the interlamellar porous carbon structure can provide efficient lithium-ion transport pathways which readily facilitate lithium-ion transport within the entire sulfur cathode. Moreover, polar bentonite aluminosilicate sheets and N-doped carbon can effectively prevent the migration of dissolved LiPSs in the cathode region, thus effectively inhibiting the shuttle effect during the long-term cycling.

3.2 Morphology and structure characterization

The morphologies of Raw-Bent, Al/CS-Bent, Bent@C, and S/Bent@C samples are shown in Figure 2. The Raw-Bent is revealed to be aggregates of lamellar particles with a porous structure (Figure 2a). After the intercalation process with Al Keggion ions and CS, the morphology become more porous and rougher, with many relatively small particles becoming visible (Figure 2b). Upon coating with carbon, the morphology of the material becomes very smooth (Figure 2c) due to the uniform structure of the PDA-C [25]. The TEM images (Figure 2e and Figure S1) further confirm the presence of a uniform carbon coating layer with a thickness of ~10 nm on the surface of Al/CS-Bent. With a high sulfur content of 80%, some agglomeration is observed in the SEM image of S/Bent@C (Figure 2d), indicating that the sulfur exists both inside the pores and outside on the surface of bentonite as the pore volume of the modified bentonite is still not enough for such high sulfur content. The TEM images (Figure 2f and Figure S2) further reveal the nanostructure of S/Bent@C, showing

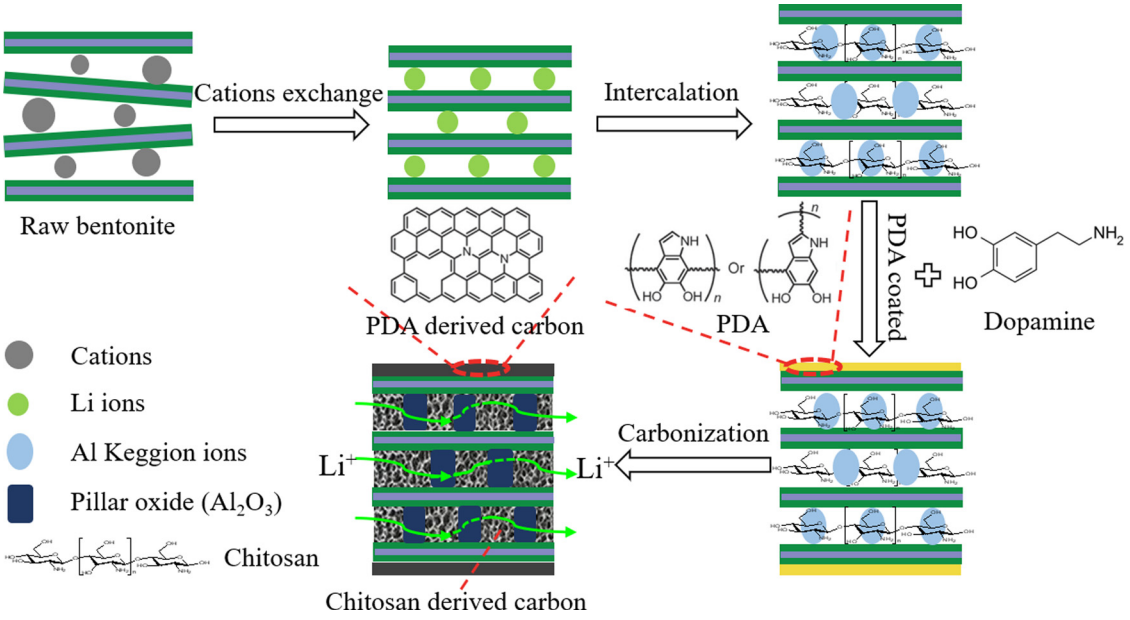

Figure 1: Schematic illustration of the synthesis of Bent@C host materials for sulfur cathodes.

that the bentonite still has a superwide interlayer distance of 0.77 nm after the diffusion of melted sulfur into Bent@C. Taking into account the thickness of the bentonite aluminosilicate layer (~0.96 nm) [26], the corresponding basal spacing is 1.73 nm. The TEM images also show that the impregnated sulfur is well-distributed with little

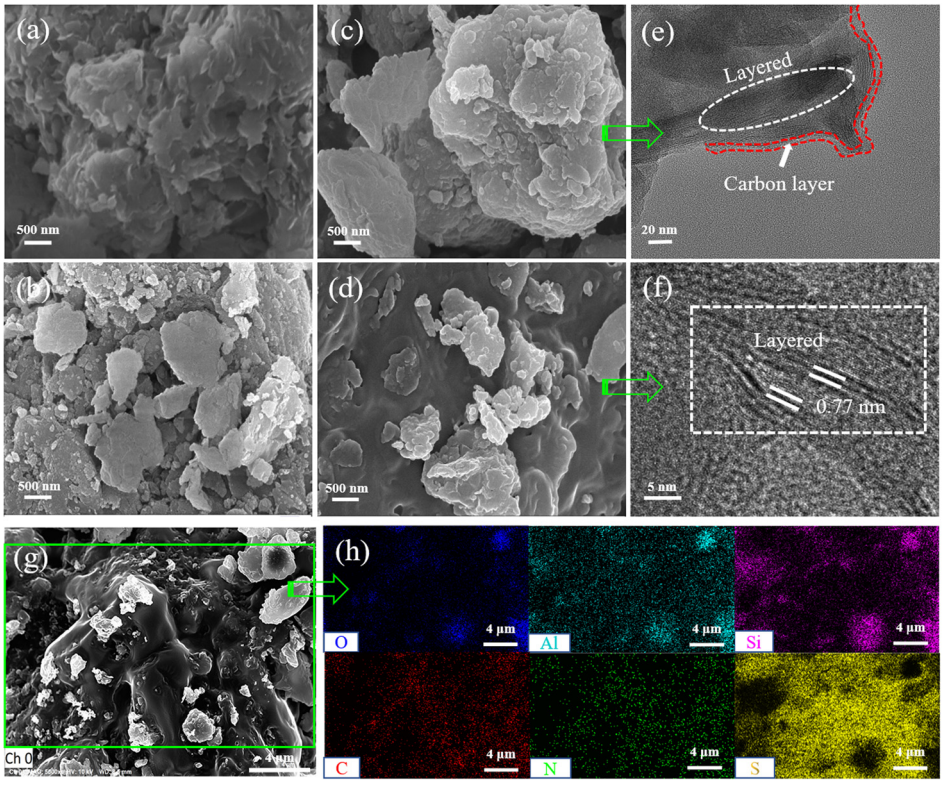

Figure 2: SEM images of Raw-Bent (a), Al/CS-Bent (b), Bent@C (c), S/Bent@C (d), and corresponding elemental mapping images of O, Al, Si, C, N, and S (g and h). TEM images of Bent@C (e) and S/Bent@C (f).

agglomeration. The element mapping of the S/Bent@C composite (Figure 2g and h) further demonstrates a homogeneous distribution of oxygen, aluminium, silicon, carbon, nitrogen, and sulfur within the material, which also confirms the successful formation of a N-doped carbon-coated structure on the intercalated-bentonite.

The XRD patterns of Raw-Bent, Li-Bent, Al/CS-Bent, and calcined Al/CS-Bent are shown in Figure 3a. The Raw-Bent exhibits the strongest (001) reflection at 2θ = 5.81°, corresponding to a basal spacing of 1.52 nm. As lithium ions are smaller than the interlamellar cations of Raw-Bent, the Li-Bent shows a (001) reflection peak at 2θ = 7.12° which is associated with a smaller basal spacing of 1.24 nm, and this value is very close to the characteristic basal spacing of sodium bentonite studied in our previous work [27]. After intercalated by Al Keggion ions and CS, the basal spacing increases significantly, which is reflected by the shift of the (001) reflection peak of Al/CS-Bent to a lower position (2θ = 4.52°). Specifically, the basal spacing of the Al/CS-Bent is determined to be 1.95 nm. However, after calcination, the (001) reflection peak is observed at 2θ = 5.06°, implying a decreased basal spacing (1.75 nm) which is caused by sintering of the particles at high temperature. In spite of the decrease, the layered structure is well-retained and the basal spacing of 1.75 nm is still desirable for the construction of efficient ion transport pathways in the interlayer of bentonite. The efficient ion transport pathways will provide S/Bent@C with fast ion diffusion and exchange properties that greatly improve the rate performance even with high sulfur loading [13]. These XRD data are highly consistent with the TEM results shown in Figure 2f.

In order to further understand the effect of intercalation on the porous structure of bentonite, nitrogen adsorption/desorption tests were performed. The nitrogen adsorption–desorption isotherms of the raw and modified bentonite samples are shown in Figure 3b. All curves are of type II adsorption isotherm exhibiting typical H3 type hysteresis loops according to the IUPAC classification. The results represent a typical behavior of slit-shaped pores,

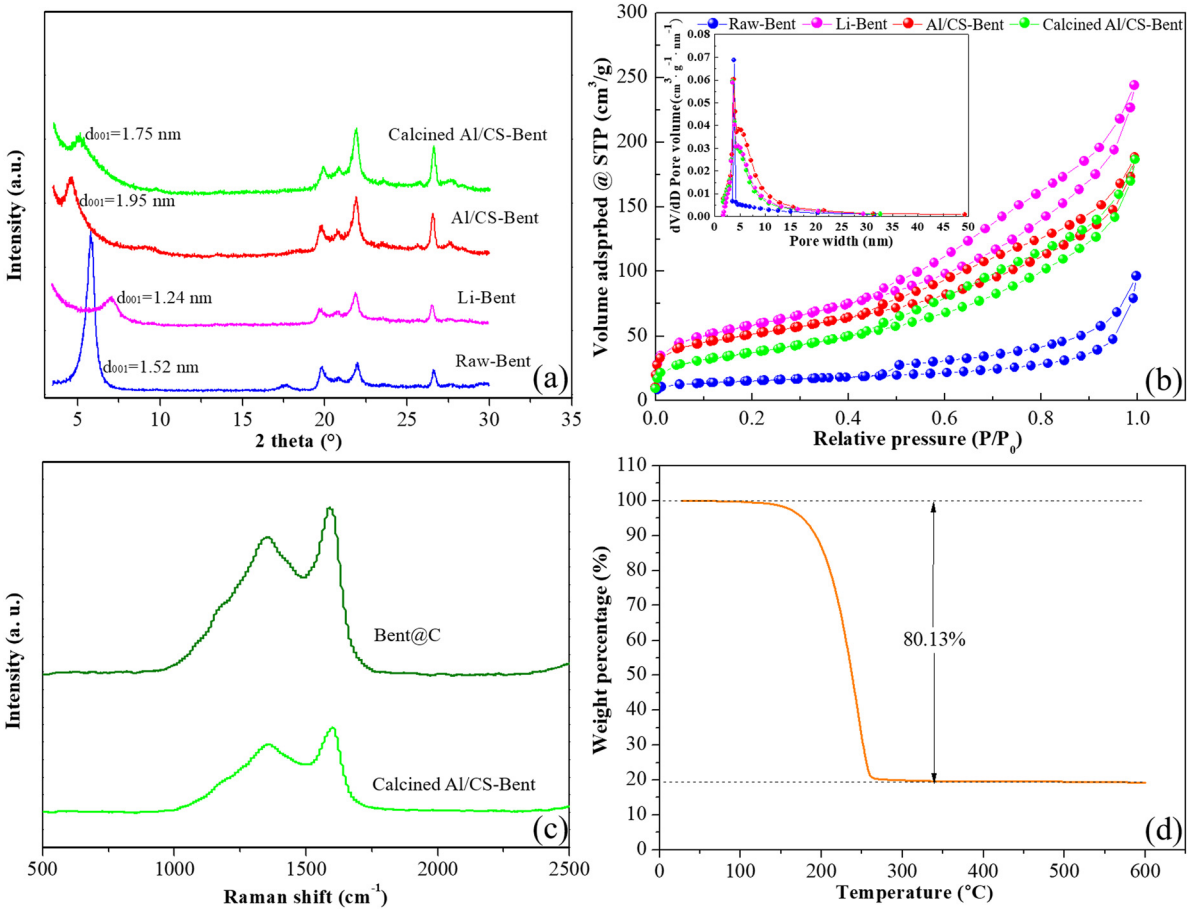

Figure 3: (a) XRD patterns; (b) nitrogen adsorption-desorption isotherms and pore size distributions (inset) of raw and modified bentonite; (c) Raman spectra of Bent@C and calcined Al/CS-Bent. (d) TG curve of S/Bent@C.

and it is evident that the configuration of parallel plates of clay minerals is fairly preserved [28]. Meanwhile, this type of adsorption–desorption isotherm indicates multilayer nitrogen adsorption and capillary condensation within the mesopores of the clay samples [28]. As illustrated in Figure 3b, raw bentonite has a monomodal distribution of pore diameters centered at ~3.0 nm. After modification via acid leaching and lithium-ion exchange, numerous pores with diameters of 4–15 nm are formed and the distribution of the pore diameters is broadened. The pore diameter further increases with inorganic/organic intercalation due to interlamellar expansion of the bentonite as the larger inorganic/organic cations (or molecules) often act as "pillars" to support the aluminosilicate sheets apart [29]. After calcination at elevated temperatures, the pore size distribution curve shifts to the left slightly and the amount of micropores increases, which could be attributed to the conversion of CS to microporous carbon in the bentonite host. This nanoporous conductive architecture can provide both nanoporous channels for low-resistant ion diffusion and nano-sized skeletons for fast electron transfer [30].

Table 1 shows the textural properties including the BET surface area (S_{BET}), pore diameter, and pore volume assigned to the raw and modified bentonite samples. The S_{BET} and pore volume of Li-Bent are much higher than that of the raw bentonite, which is caused by the open edges of the clay crystals and the removal of impurities from the interlayer of bentonite by the acid leaching process [31]. Although the basal spacing of Li-Bent increases significantly after intercalation by Al Keggion ions and CS, the S_{BET} and pore volume decrease. This may be attributed to the pore blocking effect, as a larger exchange cation/molecule (Al Keggion ions and CS) may clog some of the smaller pores [29]. The calcination process causes partial destruction of the pore structure at high temperature, resulting in a reduced S_{BET} of the intercalated-bentonite from 178.1 to 133.8 m^2/g. This is consistent with the reduction of basal spacing as calculated based on XRD results. Meanwhile, the total pore volume increases slightly while the pore diameter decreases, further suggesting the formation of porous carbon with abundant micropores.

Raman spectra of Bent@C and calcined Al/CS-Bent were recorded to gain further insight regarding the structure of the composites. As shown in Figure 3c, the Bent@C composites exhibit a typical D peak at 1,353 cm^{-1} (defects and disorder in carbon) and a G peak at 1,590 cm^{-1} (corresponding to the stretching mode of C–C bonds of typical graphite) [32]. Meanwhile, the calcined Al/CS-Bent sample has a very similar peak appearance and the D and G peaks

Table 1: Pore structure characteristics obtained from conventional analysis of nitrogen isotherms

Sample	S_{BET} (m^2/g)	Pore diameter (nm)	Pore volume (cm^3/g)
Raw-Bent	50.8	5.75	0.10
Li-Bent	204.7	7.27	0.22
Al/CS-Bent	178.1	9.21	0.24
Calcined Al/CS-Bent	133.8	6.60	0.25

are observed at 1,356 and 1,606 cm^{-1}, respectively. The ratio of the integrated intensity of the D band and the G band (I_D/I_G) are 2.46 and 2.85 for Bent@C and calcined Al/CS-Bent composites, respectively, demonstrating that the PDA- and CS-derived carbon has a significant number of defects and edges attributed to the highly porous structure and abundant nitrogen doping [23,33].

TGA was used to measure the sulfur content in the S/Bent@C composite materials. The TG curve of S/Bent@C (Figure 3d) displays a noticeable weight loss of 80.13 wt% resulting from the evaporation of sulfur. The sulfur content determined by TGA is basically in accordance with the initial addition amount of sulfur for the preparation of S/Bent@C.

The element composition, bond state, and valence state of the S/Bent@C composite were analyzed by XPS, and the results are shown in Figure 4. In the XPS survey spectra, the Al2p, Si2p, S2p, C1s, N1s, and O1s peaks are detected at the respective binding energies of 74.86, 103.04, 163.91, 284.8, 400.46, and 532.15 eV (Figure 4a). As demonstrated in Figure 4b, the C1s band in the high-resolution spectrum can be deconvoluted into three peaks at 284.8, 285.5, and 288.5 eV, corresponding to C=C/C–C, C–N, and O–C=O moieties, respectively [34,35]. The existence of C–N bonding peak further confirms the successful doping of N into the conductive carbon layer. As for the N1s spectrum (Figure 4c), it can be deconvoluted into three peaks at 398.5, 400.1, and 401.7 eV, which are respectively assigned to pyridinic-N, pyrrolic-N, and graphitic-N [34]. As shown in Figure 4d, the two peaks at 163.9 and 165.1 eV divided from the S2p spectrum are assigned to sulfur from S–S bonds [36]. Moreover, the S2p spectrum exhibits a clear peak at 168.9 eV corresponding to sulfur–oxygen (S–O) bond, which plays a critical role in the immobilization of sulfur in S/Bent@C composites [34]. The presence of S–O bond demonstrates that the oxygen-containing groups in PDA-C and bentonite aluminosilicate sheets can bond with sulfur species to promote the sulfur affinity of the electrode [37].

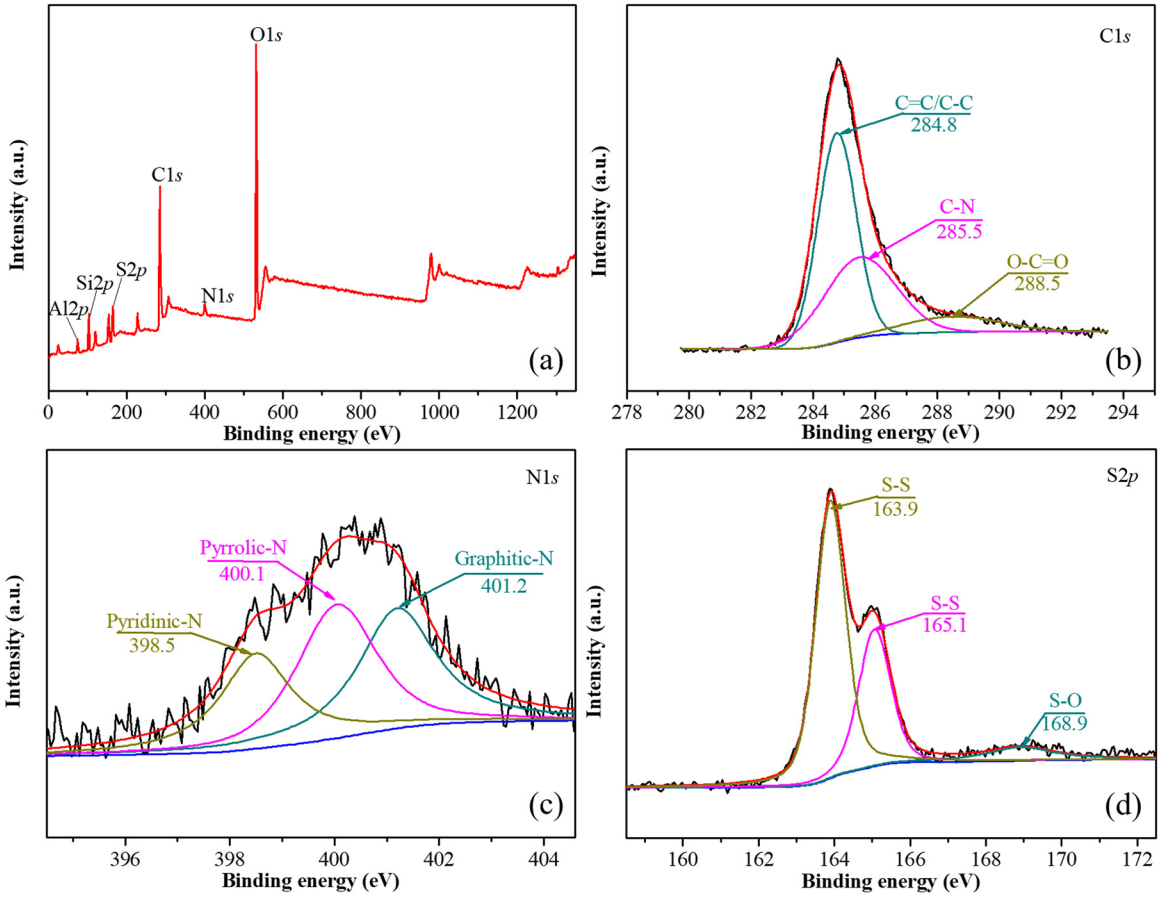

Figure 4: (a) XPS spectrum of S/Bent@C. (b–d) High-resolution XPS spectra of C1s, N1s, and S2p.

3.3 Polysulfide adsorption

In order to further prove the effective trapping of LiPSs by Bent@C, adsorption experiments were performed and photographs demonstrating the adsorption performance are shown in the insets of Figure 5. Specifically, the same amount of PDA-C, Li-Bent, and Bent@C were immersed in a Li_2S_6 solution for 12 h. The color of the Li_2S_6 solution becomes almost transparent after exposure to Bent@C and Li-Bent, while it only fades slightly from dark brown to light brown after exposure to PDA-C. The strong adsorption capacities of Li-Bent and Bent@C are further verified by ultraviolet-visible (UV-vis) spectroscopy where the absorbance corresponding to Li_2S_6 observed in the 300–400 nm region is negligible. In contrast, a strong absorbance corresponding to Li_2S_6 is seen for the solution exposed to PDA-C. The results of the adsorption experiments demonstrate that the N-doped carbon derived from PDA has a certain absorbing capacity for LiPSs, but not as strong as those of the Lewis acid sites on the broken edges of the bentonite aluminosilicate sheets.

3.4 Electrochemical performance

The electrochemical performance of S/Bent@C was investigated in Li–S batteries with lithium metal serving as the anodes. CV tests were conducted at a scan rate of 0.1 mV s^{-1} within the voltage range of 1.5–3.0 V (vs Li/Li^+). As shown in Figure 6a, S/Li-Bent exhibits two typical reduction peaks at 2.31 and 2.04 V, which are assigned to the multistep reduction process (i.e., from solid sulfur to soluble long-chain LiPSs (Li_2S_x; x = 8, 6, 4) and finally to the end-product Li_2S_2/Li_2S). In the subsequent charging process, the peak at 2.38 V is assigned to the reversible oxidation process (i.e., from Li_2S/Li_2S_2 to LiPSs and eventually back to solid sulfur) [38]. Compared to S/Li-Bent, the redox peaks of S/Bent@C shift to 2.34/2.08 and 2.35 V, respectively. Moreover, the redox peaks of S/Bent@C are stronger and sharper than that of S/Li-Bent. Such a peak appearance of S/Bent@C indicates that the electrochemical polarization of the electrode is effectively mitigated, and the redox kinetics are enhanced [39].

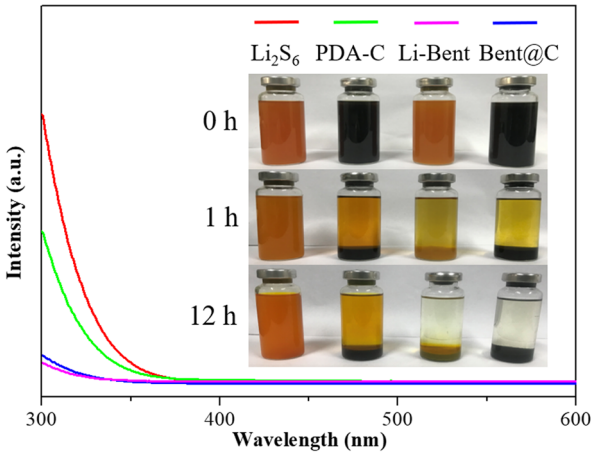

Figure 5: UV-vis spectra (300–600 nm) of the Li_2S_6 solution after exposure to PDA-C, Li-Bent, and Bent@C, respectively, for 12 h. The inset images show the color changes of the Li_2S_6 solution during exposure to different sorbent materials.

The cycle voltammograms of S/Bent@C and S/Li-Bent were further recorded at different scanning rates ranging from 0.1 to 1.2 mV s^{-1} (Figure 6b and Figure S3). At all scan rates, both S/Bent@C and Li-Bent/S show two reduction peaks and one oxidation peak. In addition, with the increasing scan rate, the reduction peaks shift to a lower voltage, while the oxidation peaks shift in the opposite direction. As the polysulfide conversion in a Li–S battery is a diffusion-limited process, all the peak currents (I_{C1}, I_{C2}, and I_A) are linear with the square root of scan rates, from which the lithium-ion diffusion rate can be estimated by using the classical Randles–Sevcik equation [40].

$$I_P = 2.69 \times 10^5 n^{3/2} A D_{Li}^{1/2} V^{1/2} \Delta C_{Li}$$

where I_P is the cathodic/anodic peak current, n is the charge transfer number, A is the active electrode area, D_{Li} is the lithium-ion diffusion coefficient, V is the scan rate, and ΔC_{Li} is the change of the lithium-ion concentration corresponding to the electrochemical reactions.

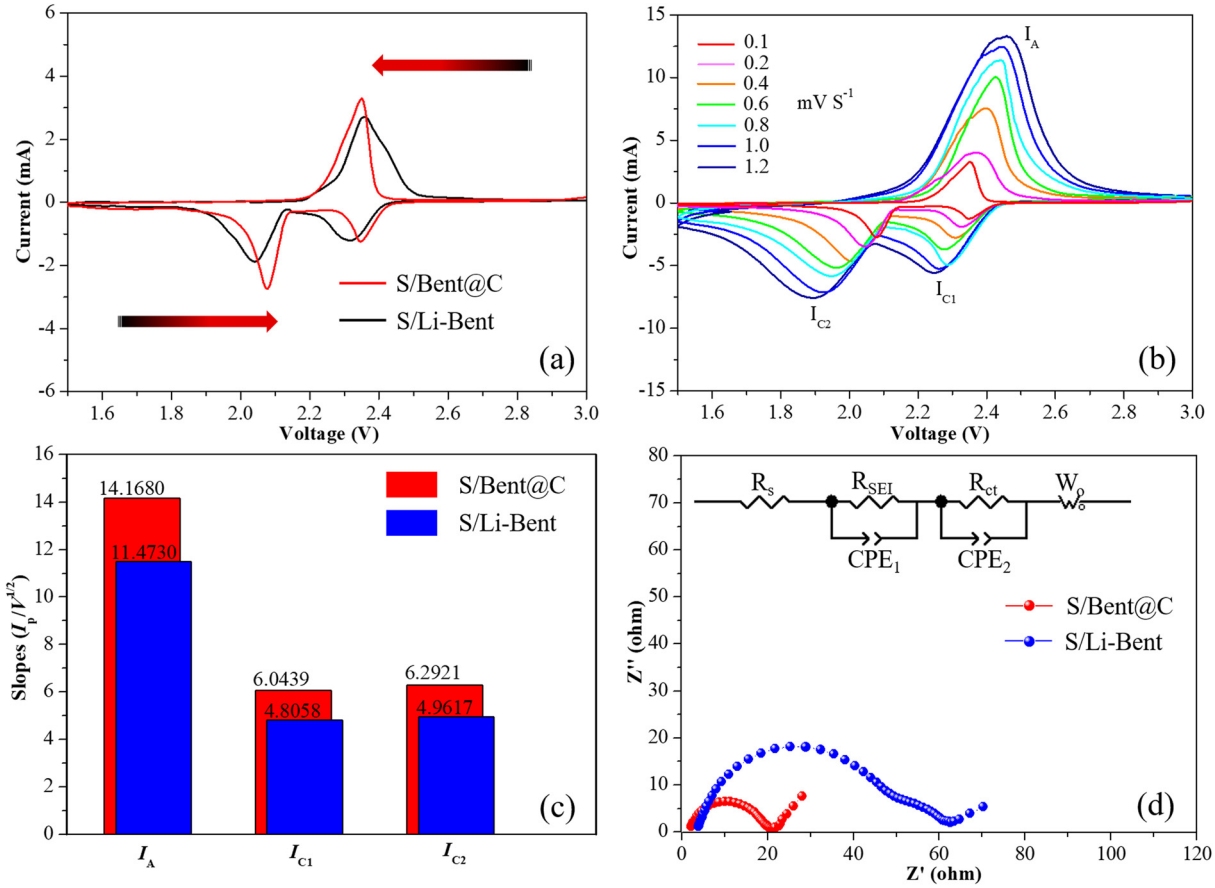

Figure 6: (a) CV curves of S/Bent@C and S/Li-Bent batteries at the scan rate of 0.1 mV s^{-1}. (b) CV curves of S/Bent@C battery under different scan rates ranging from 0.1 to 1.2 mV s^{-1}. (c) The value of $I_P/V^{1/2}$ from Figure S4 that represents the lithium-ion diffusion capability. (d) EIS curves and the equivalent circuit (inset) of S/Bent@C and S/Li-Bent batteries.

Since the values of n, A, and ΔC_{Li} are constant, the slopes of the $I_P - V^{1/2}$ lines are positively correlated to the corresponding lithium-ion diffusion rate [40]. Clearly, the S/Bent@C cathode exhibits larger slopes (K_A = 14.1680; K_{C2} = 6.2921; K_{C1} = 6.0439) than the S/Li-Bent cathode (K_A = 11.4730; K_{C2} = 4.8058; K_{C1} = 4.9617) (Figure 6c and Figure S4), indicating a much faster diffusion and reaction kinetics of S/Bent@C compared with that of

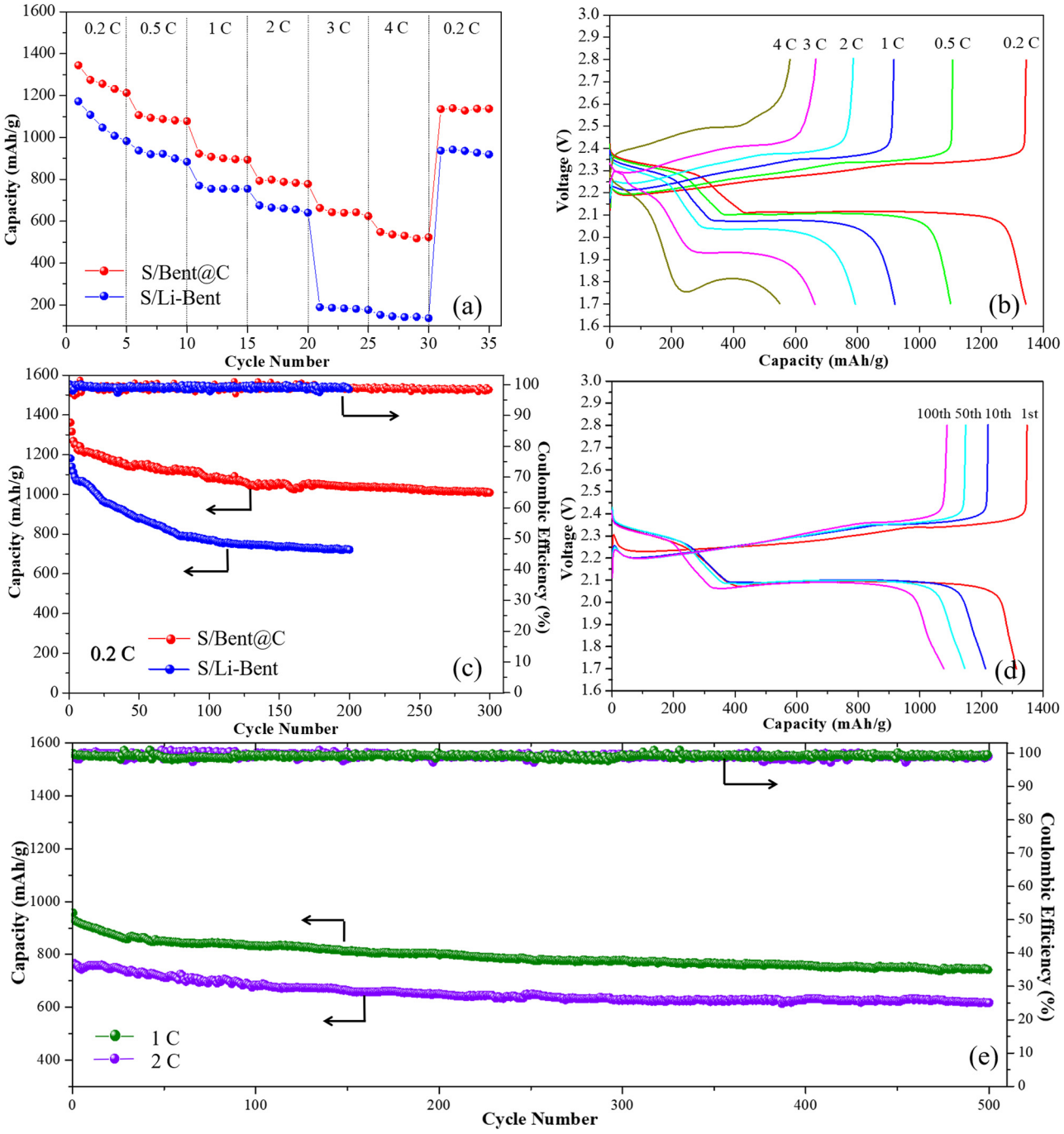

Figure 7: (a) Rate performances of S/Bent@C and Li-Bent/S electrodes with a sulfur loading of 1.2 mg cm^{-2}. (b) Galvanostatic charge/discharge profiles of S/Bent@C electrode with a sulfur loading of 1.2 mg cm^{-2} at various C-rates. (c) Cycling performances of S/Bent@C and Li-Bent/S electrodes with a sulfur loading of 2 mg cm^{-2} at 0.2C. (d) Galvanostatic charge/discharge profiles of S/Bent@C electrode with a sulfur loading of 2 mg cm^{-2} at different cycles. (e) Long-term cycling performance of S/Bent@C electrode with a sulfur loading of 2 mg cm^{-2} at 1 and 2C.

S/Li-Bent cathode [13]. The results of CV tests clearly verify that the lithium-ion diffusion rate is promoted and the electron transfer barrier is reduced, owing to the construction of ion transport pathways and conductive networks in the composite S/Bent@C cathode.

The resistance performance of batteries based on S/Bent@C and S/Li-Bent cathodes was further investigated via EIS (Figure 6d). The inset shows the equivalent circuits corresponding to these two batteries. According to the fitting results, the ohmic resistances (R_s) correspond to the total resistances of the electrodes, current collectors, electrolyte and separator, the charge transfer resistance (R_{ct}) related to the interfacial phenomena and reactions between electrode and electrolyte, and the solid electrolyte interface resistance (R_{SEI}) [41,42] were obtained, and the values are listed in Table S1. The S/Li-Bent battery exhibits much higher R_s, R_{SEI}, and R_{ct} values due to the poorer electrical conductivity of Li-Bent compared with Bent@C [43]. In addition, the oblique line at the area of low frequency represents the Warburg resistance which reflects the ion diffusion properties [44,45]. The S/Bent@C cathode shows a higher Warburg slope than that of Li-Bent cathode, indicating that the S/Bent@C cathode has facilitated ion diffusion behavior.

The rate performance was investigated by galvanostatic charge/discharge tests at various current rates. As shown in Figure 7a, the S/Bent@C cathode exhibits a constantly higher specific discharge capacity than the Li-Bent/S cathode along with the increase of the current rate from 0.2 to 0.5, 1, 2, 3, and 4C, with the average reversible capacities of 1263.8, 1089.1, 903.8, 787.6, 642.6, and 531.3 mA h g^{-1}, respectively. When the current density recovers to 0.1C, a high discharge capacity of 1135.2 mA h g^{-1} can be restored, revealing a superior rate capability and reversible performance at high-rate conditions. In addition, the corresponding charge and discharge profiles are shown in Figure 7b and Figure S5. A certain charge and discharge platform effect is maintained for the S/Bent@C cathode even at a high current rate of 4C, indicating that the electrochemical reactions from sulfur to long-chain LiPSs and then to Li_2S_2/Li_2S are continued to be effective and suggesting a kinetically efficient reaction process with a small barrier [39]. However, once the current rate increases to 3C (Figure S5a), the galvanostatic charge/discharge profiles of S/Li-Bent cathode exhibit distinct distortion and overpotential and the charge and discharge platform effect even disappears. These phenomena confirm that the free ion/electron transport, induced by the efficient ion transport pathways in the interlayer of bentonite combined with the high electronic conductivity of the interconnected 3D conductive carbon networks, confers fast redox kinetics and high sulfur utilization to the S/Bent@C cathode [41].

The cycling performances of S/Bent@C and S/Li-Bent cathodes at the current rate of 0.2C are shown in Figure 7c. The S/Bent@C cathode displays a much higher initial discharge capacity of 1,361 mA h g^{-1} compared with that of the Li-Bent/S cathode (1181.60 mA h g^{-1}). After 200 cycles, the discharge capacities of the S/Bent@C and Li-Bent/S cathodes decrease to 1039.4 and 722.20 mA h g^{-1}, respectively, and the S/Bent@C cathode retains ~74% of the starting capacity over 300 cycles. Meanwhile, the S/Bent@C cathode also maintains a constantly high coulombic efficiency of over 98% upon 300 cycles. Furthermore, Figure 7d and Figure S5b show the galvanostatic charge/discharge profiles of S/Bent@C and S/Li-Bent

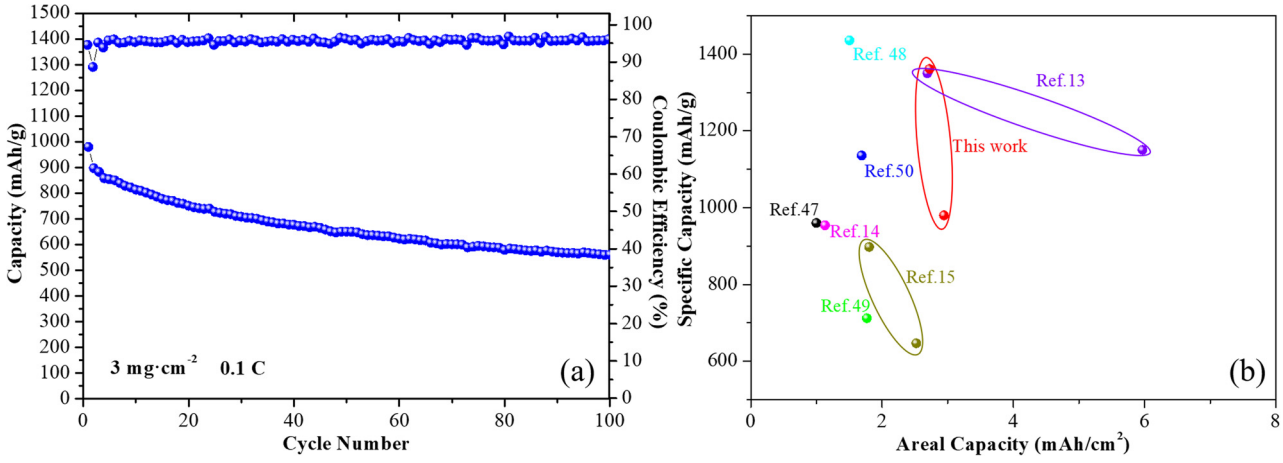

Figure 8: (a) Cycling performance of S/Bent@C electrode with a sulfur loading of 3 mg cm^{-2} at 0.1C. (b) Areal capacity and specific capacity comparisons between the Li–S battery in this work and recently reported Li–S batteries based on clay host materials [13–15,47–50].

cathodes at different cycles. With the increase of cycle number, obvious overpotential can be observed for S/Li-Bent, while S/Bent@C displays a much lower overpotential. These results strongly indicate that the Bent@C host material has a superior structure which suppresses the shuttle effect, reduces the surface passivation, and enhances sulfur reaction reversibility, owing to the combination of strong chemical sulfur confinement and free ion/electron transport.

Figure 7e displays the long-term cycling performances of the S/Bent@C cathodes at higher current densities. After 500 cycles at 1 and 2C, the S/Bent@C cathode still delivers high capacities of 743.3 and 618.1 mA h g^{-1}, with only 0.045 and 0.039% capacity decay per cycle, respectively. Besides, under higher sulfur loading, the S/Bent@C cathode also exhibits excellent cycle performances. As shown in Figure 8a, with a sulfur loading of 3 mg cm^{-2}, the S/Bent@C cathode can reveal discharge capacities of 560.2 mA h g^{-1} after 100 cycles, suggesting that a kinetically efficient reaction process occurs with a small energy barrier for free diffusion of lithium ions toward the interior of the electrode [46]. The electrochemical performance parameters of recently reported Li–S batteries based on different clay host materials were summarized in Figure 8b. Among them, Ref. [13] reported a high areal capacity up to ~6 mA h/cm^2 based on bentonite. The areal capacities were all lower than 3 mA h/cm^2 based on the other types of clays [14,15,47–50]. Our current work provided a highly competitive performance, but high sulfur loading (>3 mg/cm^2) cathodes are needed to be further studied.

The above experimental results show that Bent@C is an ideal host material, providing plentiful efficient lithium-ion transport pathways for promoting ion transport, improving electron transport through the interconnected 3D conductive carbon network, and trapping soluble LiPSs via Lewis acid-base interactions as well as N-doped carbon, thus resulting in enhanced redox kinetics and improved rate/cycle performances.

4 Conclusions

In summary, the use of the modified bentonite clay as a sulfur host is proposed herein to resolve the shuttle effect of the LiPS and to promote lithium-ion transport in the cathodes of Li–S batteries. In order to enhance the conductivity of bentonite host, N-doped conductive carbon is not only deposited onto the surface of bentonite through PDA-C coatings, but also introduced into the interlayer spaces of bentonite through the intercalation-carbonization of chitosan. In the meantime, the efficient ion transport pathways in the interlayer of bentonite are controllably constructed via the inorganic/organic intercalation process, which improves the lithium-ion diffusion efficiency and facilitates energy conversion via sulfur redox reactions. Therefore, the S/Bent@C cathode, with the N-doped carbon-coated intercalated-bentonite as the sulfur host materials, provides improved rate capabilities and cycling stability compared with the Li-Bent/S cathode which employs lithium-bentonite as the sulfur host. This work would broaden the applicability of bentonite clay in energy storage and provide an economical and efficient host material for the design of advanced Li–S batteries.

Acknowledgments: The authors thank Tengyou Wei, Professor of Chemical Engineering at Guangxi University, for his helpful discussions of the modification study of the bentonite host.

Funding information: This work was financially supported by the China Postdoctoral Science Foundation (Grant No. 2020M672549), the National Natural Science Foundation of China (Grant No. 52003111), and the GDAS' Project of Science and Technology Development (Grant Nos. 2021GDASYL-20210103097, 2020GDASYL-20200102029, and 2020GDASYL-20200102028).

Author contributions: All authors have accepted responsibility for the entire content of this manuscript and approved its submission.

Conflict of interest: The authors state no conflict of interest.

References

[1] Yang X, Peng Y, Hou J, Liu Y, Jian X. A review for modified Li composite anode: principle, preparation and challenge. Nanotechnol Rev. 2020;9(1):1610–24.
[2] Zhou L, Danilov DL, Eichel RA, Notten PHL. Host materials anchoring polysulfides in Li–S batteries reviewed. Adv Energy Mater. 2020;20:2001304.
[3] Huang J, Lin Y, Yu J, Li D, Du J, Yang B, et al. N-doped foam flame retardant polystyrene derived porous carbon as an efficient scaffold for lithium-selenium battery with long-term cycling performance. Chem Eng J. 2018;350:411–8.
[4] Wang R, Yang J, Chen X, Zhao Y, Zhao W, Qian G, et al. Highly dispersed cobalt clusters in nitrogen-doped porous carbon enable multiple effects for high performance Li–S battery. Adv Energy Mater. 2020;10(9):1903550.

[5] Zhang J, Huang Z, He C, Zhang J, Mei P, Han X, et al. Binary carbon-based additives in $LiFePO_4$ cathode with favorable lithium storage. Nanotechnol Rev. 2020;9(1):934–44.
[6] Li MY, Carter R, Douglas A, Oakes L, Pint CL. Sulfur vapor-infiltrated 3D carbon nanotube foam for binder-free high areal capacity lithium sulfur battery composite cathodes. ACS Nano. 2017;11(5):4877–84.
[7] Wu Z, Yuan L, Han Q, Lan Y, Zhou Y, Jiang X, et al. Phosphorous/oxygen co-doped mesoporous carbon bowls as sulfur host for high performance lithium–sulfur batteries. J Power Sources. 2020;450:227658.
[8] Ye Y, Wu F, Liu Y, Zhao T, Qian J, Xing Y, et al. Toward practical high-energy batteries: a modular assembled oval-like carbon microstructure for thick sulfur electrodes. Adv Mater. 2017;29(48):1700598.
[9] Zheng Y, Zheng S, Xue H, Pang H. Metal-organic frameworks for lithium–sulfur batteries. J Mater Chem A. 2019;7(8):3469–91.
[10] Wang C, Yi Y, Li H, Wu P, Li M, Jiang W, et al. Rapid gas-assisted exfoliation promises V_2O_5 nanosheets for high performance lithium–sulfur batteries. Nano Energy. 2020;67:104253.
[11] Pang J, Mendes RG, Bachmatiuk A, Zhao L, Ta HQ, Gemming T, et al. Applications of 2D MXenes in energy conversion and storage systems. Chem Soc Rev. 2019;48(1):72–133.
[12] Liu Y, Jiang L, Wang H, Wang H, Jiao W, Chen G, et al. A brief review for fluorinated carbon: synthesis, properties and applications. Nanotechnol Rev. 2020;8(1):573–86.
[13] Chen W, Lei T, Lv W, Hu Y, Yan Y, Jiao Y, et al. Atomic interlamellar ion path in high sulfur content lithium-montmorillonite host enables high-rate and stable lithium–sulfur battery. Adv Mater. 2018;30(40):1804084.
[14] Wang Y, Wang X, Ye H, Han K. Carbon coated halloysite nanotubes as efficient sulfur host materials for lithium sulfur batteries. Appl Clay Sci. 2019;179:105172.
[15] Wu F, Lv H, Chen S, Lorger S, Srot V, Oschatz M, et al. Natural vermiculite enables high-performance in lithium–sulfur batteries via electrical double layer effects. Adv Funct Mater. 2019;29(27):1902820.
[16] Wu L, Wei T, Tong Z, Zou Y, Lin Z, Sun J. Bentonite-enhanced biodiesel production by NaOH-catalyzed transesterification of soybean oil with methanol. Fuel Process Technol. 2016;144:334–40.
[17] Sun Y, Mei J, Hu H, Ying J, Zhou W, Zhao X, et al. *In situ* polymerization of exfoliated structure PA6/organo-clay nanocomposites. Rev Adv Mater Sci. 2020;59(1):434–40.
[18] Chen W, Hu Y, Lv W, Lei T, Wang X, Li Z, et al. Lithiophilic montmorillonite serves as lithium ion reservoir to facilitate uniform lithium deposition. Nat Commun. 2019;10:4973.
[19] Zhao J, Chen D, Boateng B, Zeng G, Han Y, Zhen C, et al. Atomic interlamellar ion path in polymeric separator enables long-life and dendrite-free anode in lithium ion batteries. J Power Sources. 2020;451:227773.
[20] Jian X, Wang H, Rao G, Jiang L, Wang H, Subramaniyam CM, et al. Self-tunable ultrathin carbon nanocups as the electrode material of sodium-ion batteries with unprecedented capacity and stability. Chem Eng J. 2019;364:578–88.
[21] Zhu J, Wen K, Wang Y, Ma L, Su X, Zhu R, et al. Superior thermal stability of Keggin-Al30 pillared montmorillonite: a comparative study with Keggin-Al13 pillared montmorillonite. Microporous Mesoporous Mater. 2018;265:104–11.
[22] Darder M, Colilla M, Ruiz-Hitzky E. Biopolymer-clay nanocomposites based on chitosan intercalated in montmorillonite. Chem Mater. 2003;15(20):3774–80.
[23] Gu H, Xu X, Dong M, Xie P, Shao Q, Fan R, et al. Carbon nanospheres induced high negative permittivity in nanosilver polydopamine metacomposites. Carbon. 2019;147:550–8.
[24] Zhang LL, Ma D, Li T, Liu J, Ding XK, Huang YH, et al. Polydopamine-derived nitrogen-doped carbon-covered $Na_3V_2(PO_4)_2F_3$ cathode material for high-performance Na-ion batteries. ACS Appl Mater Interfaces. 2018;10(43):36851–9.
[25] Li R, Parvez K, Hinkel F, Feng X, Müllen K. Bioinspired wafer-scale production of highly stretchable carbon films for transparent conductive electrodes. Angew Chem Int Ed. 2013;52(21):5535–8.
[26] Chen B, Zhu L, Zhu J. Configurations of the bentonite-sorbed myristylpyridinium cation and their influences on the uptake of organic compounds. Env Sci Technol. 2005;39(16):6093–100.
[27] Zhao H, Liao B, Nian F, Wang K, Guo Y, Pang H. Investigation of the clay sensitivity and cement hydration process of modified HPEG-type polycarboxylate superplasticizers. J Appl Polym Sci. 2018;135(32):46572.
[28] Banković P, Milutinović-Nikolić A, Mojović Z, Jović-Jovičić N, Perović M, Spasojević V, et al. Synthesis and characterization of bentonites rich in beidellite with incorporated Al or Al-Fe oxide pillars. Microporous Mesoporous Mater. 2013;165:247–56.
[29] Lee JF, Lee CK, Juang LC. Size effects of exchange cation on the pore structure and surface fractality of montmorillonite. J Colloid Interface Sci. 1999;217(1):172–6.
[30] Zeng W, Shu L, Li Q, Chen S, Wang F, Tao XM. Fiber-based wearable electronics: a review of materials, fabrication, devices, and applications. Adv Mater. 2014;26(31):5310–36.
[31] Komadel P. Acid activated clays: materials in continuous demand. Appl Clay Sci. 2016;131:84–99.
[32] Ghouri ZK, Motlak M, Afaq S, Barakat NAM, Abdala A. Template-free synthesis of Se-nanorods-rGO nanocomposite for application in supercapacitors. Nanotechnol Rev. 2019;8(1):661–70.
[33] Tian W, Zhang X, Guo Y, Mu C, Zhou P, Yin L, et al. Hybrid silica-carbon bilayers anchoring on FeSiAl surface with bifunctions of enhanced anti-corrosion and microwave absorption. Carbon. 2021;173:185–93.
[34] Zuo Y, Ren P, Zhao M, Su W, Chen Y, Tang Y, et al. Stable lithium–sulfur batteries with high sulfur content fabricated by ultralight ochroma lagopus-derived carbon with dopamine shell as sulfur host. J Alloy Comp. 2020;819:152995.
[35] Wang Y, Feng J, Jin L, Li C. Photocatalytic reduction of graphene oxide with cuprous oxide film under UV-vis irradiation. Rev Adv Mater Sci. 2020;59(1):207–14.
[36] Wang DG, Li N, Hu Y, Wan S, Song M, Yu G, et al. Highly fluoro-substituted covalent organic framework and its application in lithium–sulfur batteries. ACS Appl Mater Interfaces. 2018;10(49):42233–40.
[37] Chen H, Zhou G, Boyle D, Wan J, Wang H, Lin D, et al. Electrode design with integration of high tortuosity and sulfur-philicity for high-performance lithium–sulfur battery. Matter. 2020;2(6):1605–20.
[38] Liu S, Zhang X, Wu S, Chen X, Yang X, Yue W, et al. Crepe cake structured layered double hydroxide/sulfur/graphene as a positive electrode material for Li–S batteries. ACS Nano. 2020;14(7):8220–31.

[39] Zhou G, Liu K, Fan Y, Yuan M, Liu B, Liu W, et al. An aqueous inorganic polymer binder for high performance lithium–sulfur batteries with flame-retardant properties. ACS Cent Sci. 2018;4(2):260–7.
[40] Tao X, Wang J, Liu C, Wang H, Yao H, Zheng G, et al. Balancing surface adsorption and diffusion of lithium-polysulfides on nonconductive oxides for lithium–sulfur battery design. Nat Commun. 2016;7:11203.
[41] Lei T, Hu Y, Chen W, Lv W, Jiao Y, Wang X, et al. Genetic engineering of porous sulfur species with molecular target prevents host passivation in lithium sulfur batteries. Energy Storage Mater. 2020;26:65–72.
[42] Fu J, Ali R, Mu C, Liu Y, Mahmood N, Lau WM, et al. Large-scale preparation of 2D VSe_2 through a defect-engineering approach for efficient hydrogen evolution reaction. Chem Eng J. 2021;411:128494.
[43] Shih HJ, Chang JY, Cho CS, Li CC. Nano-carbon-fiber-penetrated sulfur crystals as potential cathode active material for high-performance lithium–sulfur batteries. Carbon. 2020;159:401–11.
[44] Lin J, Yin X, Pang H, Zhang L, Liao B, Xin M. Tuning the wrinkles in 3D graphene architectures for mass and electron transport. Adv Mater Interfaces. 2020;7(10):1902190.
[45] Lin Y, Huang J, Shi L, Cong G, Zhu C, Xu J. Combining $Zn_{0.76}Co_{0.24}S$ with S-doped graphene as high-performance anode materials for lithium and sodium-ion batteries. Nanotechnol Rev. 2020;9(1):1227–36.
[46] Zhou G, Wang DW, Li F, Hou PX, Yin L, Liu C, et al. A flexible nanostructured sulphur-carbon nanotube cathode with high rate performance for Li–S batteries. Energy Environ Sci. 2012;5(10):8901–6.
[47] Cao Z, Ma C, Jia Y, Sun Z, Yue H, Yin Y, et al. Activated clay of nest structure encapsulated sulfur cathodes for lithium–sulfur batteries. RSC Adv. 2015;5(36):28349–53.
[48] Pan J, Wu C, Cheng J, Pan Y, Ma Z, Xie S, et al. Sepiolite-sulfur as a high-capacity, high-rate performance, and low-cost cathode material for lithium–sulfur batteries. J Power Sources. 2015;293:527–32.
[49] Pei Y, Wang Y, Darraf Y, Chang AY, Zhao H, Liu X, et al. Confining sulfur particles in clay nanotubes with improved cathode performance of lithium–sulfur batteries. J Power Sources. 2020;450:227698.
[50] Cen T, Zhang Y, Tian Y, Zhang X. Synthesis and electrochemical performance of graphene@ halloysite nanotubes/sulfur composites cathode materials for lithium–sulfur batteries. Materials. 2020;13(22):5158.